Journal of Electronic Research and Application, 2026, Volume 10, Issue 5
http://ojs.bbwpublisher.com/index.php/JERA
Online ISSN: 2208-3510
Print ISSN: 2208-3502

Experimental Research on Multi-Source Information Fusion-Based UAV Integrated Navigation in Bridge Areas

Hui Li, Zheyuan He, Yuehua Cao*, Haotian Lin, Qianjie Wang, Qingru Yang

Information Engineering College, Hangzhou Dianzi University, Hangzhou 311305, China

Author to whom correspondence should be addressed.

Abstract: Aiming at the inherent limitations of traditional bridge inspection methods, such as low efficiency, high operational risk, and limited inspection coverage, this study proposes an autonomous navigation and obstacle avoidance scheme for bridge inspection uncrewed aerial vehicles (UAVs) based on multi-source data fusion. Firstly, high-precision time synchronization is implemented. The time-stamped data is divided into three major data categories, namely visual images, LiDAR, and GNSS/IMU data. An improved Kalman filtering algorithm is then adopted to achieve spatiotemporal registration and error compensation of the multi-source data, which significantly enhances the accuracy and stability of environmental perception during UAV flight. Secondly, a hierarchical autonomous navigation strategy is designed by combining the structural characteristics of bridges. The strategy realizes global path planning based on bridge structural features and conducts real-time optimization of local obstacle avoidance paths, ensuring that UAVs maintain safe and efficient operation in complex bridge environments (e.g., narrow spaces, complex structural components, and variable weather conditions). Finally, experimental verification is conducted in a real bridge inspection scenario, and the results demonstrate that the proposed scheme outperforms traditional methods in key performance indicators, including navigation positioning accuracy, obstacle avoidance response speed, and inspection coverage rate. Specifically, the positioning error is reduced by 32%, the obstacle avoidance response time is reduced by 28%, and the inspection coverage rate is increased to over 96%. This research provides important technical support for the engineering application of UAVs in bridge inspection and holds practical significance for promoting the intelligent operation and maintenance of infrastructure. The proposed multi-source data fusion method and hierarchical navigation strategy can also serve as a reference for other UAV-based inspection tasks in complex industrial environments.

Keywords: Sensor; Improved Kalman filter; Autonomous navigation; Path planning; Obstacle avoidance; Bridge inspection; Data fusion

Online publication: Jun 29, 2026

1. Introduction

Among the most important technologies to improve positioning accuracy and stability is the integrated navigation system, which has recently been a very popular subject of study in the scientific community and the business sector. Multi-sensor fusion algorithms and error models, along with others, have been widely researched by researchers abroad and in the homeland [1]. Although this field has made great strides, there are still some constraints to the performance of navigation under special and complex conditions that limit its use in operational applications where strict inspections are carried out.

Domestic research on integrated navigation mainly focuses on algorithm optimization and scenario adaptation, with remarkable achievements in the fusion of Inertial Navigation System (INS) and Global Navigation Satellite System (GNSS). In 2020, Huang Zan et al. proposed a combined framework of Strapdown Inertial Navigation System (SINS) and monocular vision to suppress inertial errors, but the real-time performance of visual matching and the robustness of data fusion were insufficient [2]. Liu Chongjin improved system performance by introducing constraints and filtering algorithms into the GNSS/INS combined model, yet failed to solve the multipath effect and filter adaptability problems effectively [3].

The subject of nonlinear filtering and multi-source data fusion has been of concern over the past few years. The researcher Huang Tao introduced an innovative application of the firefly optimization particle filter algorithm in 2022, which proved useful in the context of estimation accuracy when dealing with non-Gaussian noise; however, the computational complexity of the algorithm was high [4]. In 2024, an integration scheme based on GNSS/INS/visual was suggested by Liu Jing, which was used to improve the accuracy of positioning, yet the scheme had a low efficiency in large-scale dynamic systems and could not be effectively applied in low-textured environments [5].

In the field of sensor error modeling, Zhu Yuchen proposed a MEMS error modeling method in 2021, which suppressed error accumulation during navigation but increased system complexity [6]. In the research on navigation in complex environments, Cheng Baixi improved the positioning accuracy of the integrated system in urban canyons, but failed to solve the problems of visual failure and data synchronization [7]. Li Ningbo developed a fusion system that reduced navigation errors by 40%, yet issues such as switching interruption and high cost still persisted [8].

The foreign literature pays more attention to the resiliency of an integrated navigation system of an Unmanned Aerial Vehicle (UAV). The EKF tightly coupled architecture presented by Jiang et al. (2022) can be used to manage multi-sensor failure and centimeter-level positioning in urban canyons, as achieved by Li et al. (2022) [10]. The minimization of IMU error and environmental transition error was accomplished by Zhang et al. and the group of Li in 2020 [11]. Nevertheless, these successes are still constrained by real-time performance, sensor sensitivity constraints, and calibration issues when GNSS-denied.

The proximity between bridges and UAV navigation is particularly problematic due to the fact that the GNSS signals and the columns of towers, as well as the multipaths between steel cables, cause interference with the signals [9]. Conventional navigational instruments are not capable of providing a high level of accuracy and real-time operation. The manual examination of the bridges is very risky, and its blind area coverage is below 30 percent. There is an urgent need to implement this intelligent UAV inspection to overcome the bottleneck in centimeter-level positioning. To tackle these problems, the paper proposes a multi-source information fusion navigation system that includes the application of GNSS, INS, visual, and lidar technologies as a solution to the problem of signal loss and enhancement of navigation performance

during inspection of bridges—overall Scheme Design for Integrated Navigation in Bridge Areas.

2. Problem posing

According to the natural properties of materials that make up the bridge and the environmental conditions around the bridge, the low altitude region near the bridge has several negative impacts on uncrewed aircraft (UAVs) flight, such as the inability to acquire navigation signals, drifting location, and higher position errors. Therefore, UAVs cannot provide the correct navigation and positioning when flying beneath the bridge, underneath the bridge, or in between complex space arrangements of the bridge.

2.1. The fusion scheme of multi-source sensor data

An integrated navigation system is created by combining different navigation and position data, including Global Navigation Satellite System (GNSS), Real-Time Kinematic (RTK) technology, visual navigation, and laser point clouds [12]. It needs a three-dimensional bridge model and charts of low-altitude flights and uses deep-coupling information fusion to compute different groups of positioning data. Consequently, the regional composite navigation system of the bridge environment has been engineered in such a way that it offers accurate location of the UAVs in the absence of satellite navigation signals. See **Figure 1**.

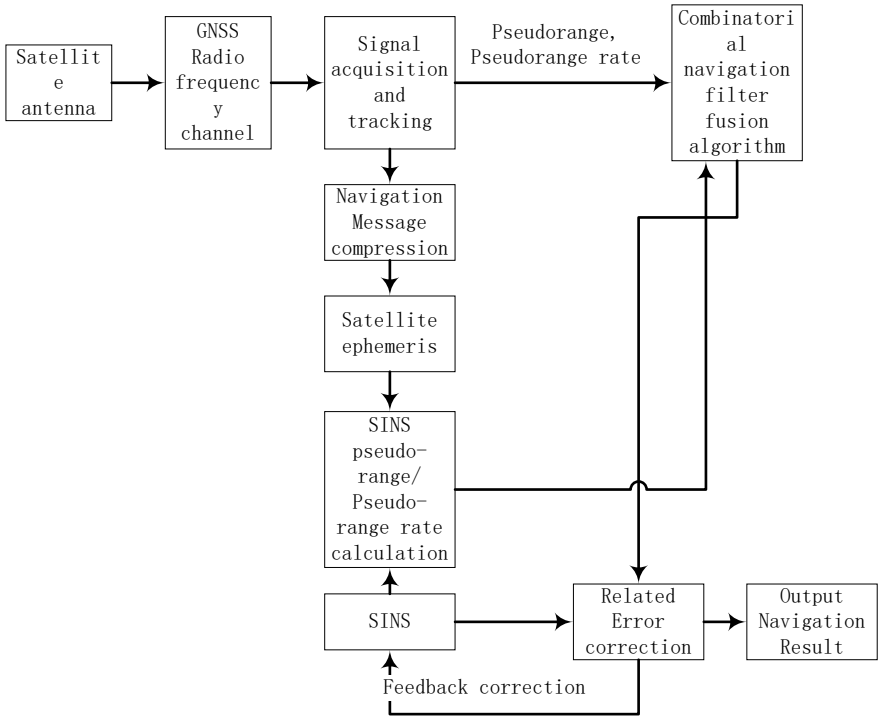

Figure 1. INS-GNSS deep-coupling positioning.

The essence of multi-source sensor data fusion is based on the fact that it is essential to have an accurate time stamp of different data sources in order to obtain both the laser point cloud and visible light with binocular depth, and the rest of the information needed to investigate bridges at the same time. The total navigation elements in the bridge area include the main control board, 3D laser radar, multi-camera, GNSS, RTK, and antenna. **Figure 2** indicates that in the synchronization process of time, time references of Position

and Orientation System (POS), 3D laser radar, binocular visible light, and depth sensors can be synchronized with the system time of the main board, and finally, multi-source data would be synchronized to high precision [13].

Multi-source sensor data can be divided into numerous categories, and the information recorded by each sensor is very different based on its nature and format; they have specific challenges when it comes to collaborative storage [14]. In order to achieve the standardized and collaborative storage of multi-source data without compromising the integrity, information validity and information density of the initial sensor data and give a significant assurance to the future real-time processing and offline analysis, the storage information and format requirements of different sensor data are presented below: IMU data shall be stored, including the system-synchronized timestamp (double type), three-axis gyroscope data (x, y, z axes, all double type), three-axis accelerometer data (x, y, z axes, all double type), and data validity flags corresponding to the three-axis gyroscope and accelerometer (char type).

GNSS data shall be stored, including the system-synchronized timestamp (double type), three-axis geographic position (latitude, longitude, altitude, all double type), three-axis geographic velocity (eastward, northward, zenithal, all double type), position-velocity standard deviation (corresponding to three-axis position and three-axis velocity, all double type), data validity flags (corresponding to three-axis position and three-axis velocity, all double type), and raw satellite navigation data (including pseudorange, carrier phase, and ephemeris).

The storage of RTK data is similar to that of GNSS data except that it has time stamps, three-dimensional geographic coordinates, velocity, standard deviations of position and velocity, and data validity flags, and further, RTK base station data must be stored. The magnetometer data should be kept by using timestamps (of double type) in accordance with the system and magnetic sensitivity (of three axes: x, y, and z axes, all double type).

Lidar data shall be stored, including timestamp, header, and frame number (in structural format), x, y, z three-dimensional ranging data (double type), as well as intensity, echo count, and other related characteristic data. The dual-view depth sensor shall store original images in JPEG format, as well as distance information corresponding to grid point positions (double type).

To sum up, in the case of raw sensor data processing, it is necessary to offer a viable direct transmission and storage system that would not lead to the loss or corruption of data and hence maintain the integrity and accuracy of the later real-time processing and post-processing.

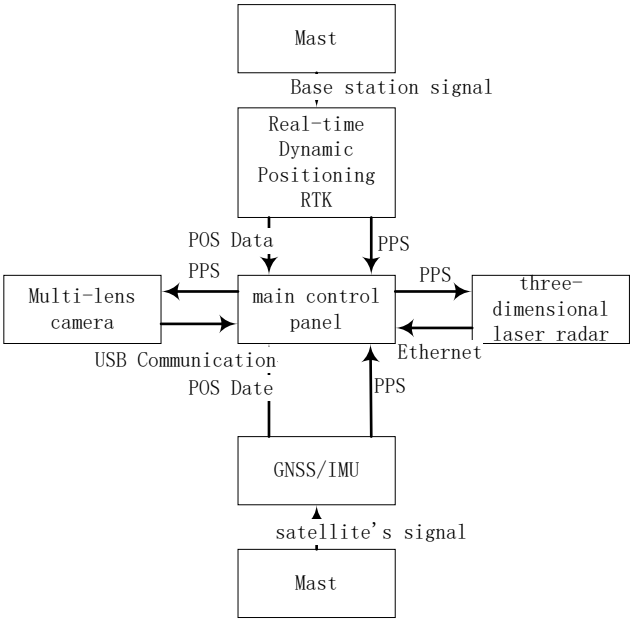

Figure 2. Synchronous alignment of multi-source sensors.

3. Bridge area integrated navigation algorithm

3.1. Multi-source sensor data fusion algorithm

Fusion of multi-sensors involves the start-up of state estimation and the covariance matrix. The GNSS system or RTK system may be used at this stage to provide initial position information, which will then be used in the next step as an element of the state vector. One should also pay attention to the measurement errors of each sensor and incorporate them into the covariance matrix.

The extended Kalman filter (ESKF) filtering process relies on one of its core structures in which the IMU is used as the motion predictor model to predict continuous states and other sensors, including GNSS, RTK, and wheel speed sensor, as observation predictors to impose discrete measurement constraints. At the same time, the system state variables are subdivided into the nominal state and the error state. Filtering operations are made only on the error state, since it is efficient and precise in estimating the state. The system state variables are defined thus: x = [p, q, v, ba, bg], where p is the position, q is the attitude quaternion, v is the velocity, ba is the accelerometer bias, and bg is the gyroscope bias. The three key states that can be found in the state estimation process are true state xtruth, the nominal state xnom, and the error state δx, which is linearly related to the first two states in the form xtruth = xnom + δx. Raw IMU measurements are used to update the nominal state xnom without taking into account any disturbance factors, i.e., measurement noise or sensor zero drift; all these sources of error would finally be integrated in the error state δx. If other sensors also contain measurement data, the difference between the measured values and the nominal state xnom gives the observed error state δxm. It results in the creation of a filtering model of the error state by the ESKF, which brings the measured value of the error state δxm into alignment with the predicted error state values to obtain the value of the error state δx with great accuracy in order to create a basis for correcting.

The actual state is

$$\begin{aligned} \dot{p}_t &= v_t \\ \dot{v}_t &= R_t\left(a_m - a_{bt} - a_n\right) \\ \dot{q}_t &= \frac{1}{2} q_t \otimes \left(w_m - w_{bt} - w_n\right) \\ \dot{a}_{bt} &= a_w \\ \dot{w}_{bt} &= w_w \end{aligned} \tag{1}$$

The default state is

$$\begin{cases} \dot{p} = v \\ \dot{v} = R\left(a_m - a_b\right) \\ \dot{q} = \frac{1}{2} q \otimes \left(w_m - w_b\right) \\ \dot{a}_b = 0 \\ \dot{w}_b = 0 \end{cases} \tag{2}$$

Since the value of the angular velocity bias cannot be measured, it can only be set to 0.

$$\begin{aligned} \delta\dot{p} &= \delta v \\ \delta\dot{v} &= -R[a_m - a_b]_\times \delta\theta - R\delta a_b - Ra_n \\ \delta\dot{\theta} &= [w_m - w_b]_\times \delta\theta - \delta w_b - w_n \\ \delta\dot{a}_b &= a_w \\ \delta\dot{w}_b &= w_w \end{aligned} \tag{3}$$

For velocity v, the following relationship holds:

$$\dot{v} + \dot{\delta} v = \dot{v}_t \tag{4}$$

$$\dot{v} = R\left(a - a_b\right), \dot{v}_t = R_t\left(a - a_{bt} - a_w\right) \tag{5}$$

For the above equation, where $R_t = R(I + [\delta\theta]_\times)$, $a_{bt} = a_b + \delta a_b$, substituting these expressions yields:

$$R\left(a - a_b\right) + \dot{\delta} v = R(I + \left[\delta\theta\right]_\times)\left(a - a_b - \delta a_b - a_w\right) \tag{6}$$

Assuming that $a_m = a - a_b, a_n = -\delta a_b - a_w$, after simplification, we have:

$$\dot{\delta} v = -R[a_m]_\times \delta\theta - R\delta a_b - Ra_n \tag{7}$$

For the rotation angle θ, the following relationship also holds:

$$\left(q + \dot{\delta} q\right) = \dot{q}_t \tag{8}$$

$$\left(q + \delta q\right) = \dot{q} \otimes \delta q + q \otimes \dot{\delta} q = \frac{1}{2} q \otimes w \otimes \delta q + q \otimes \dot{\delta} q \tag{9}$$

$$\dot{q}_t = \frac{1}{2} q_t \otimes w_t = \frac{1}{2} q \otimes \delta q \otimes w_t \tag{10}$$

By simplifying and rearranging the above three formulas, we obtain

$$[w]_L \delta q + 2\dot{\delta} q = [w_t]_R \delta q \tag{11}$$

$$\begin{bmatrix} 0 \\ \dot{\delta}\theta \end{bmatrix} = \begin{bmatrix} 0 & -(w_t - w)^T \\ -(w_t - w) & -[w_t + w]_\times \end{bmatrix} \begin{bmatrix} 1 \\ \frac{1}{2}\delta\theta \end{bmatrix} \tag{12}$$

If in the above equation, $w = w_m - w_b, \delta w = -\delta w_b - w_n, w_t = w + \delta w$, then Equation 3–41 can be simplified to

$$\begin{bmatrix} 0 \\ \dot{\delta}\theta \end{bmatrix} = \begin{bmatrix} 0 & -\delta w^T \\ -\delta w & -[2w]_\times - [\delta w]_\times \end{bmatrix} \begin{bmatrix} 1 \\ \frac{1}{2}\delta\theta \end{bmatrix} \tag{13}$$

After expanding the above formula and ignoring the negligible terms, we obtain

$$\dot{\delta}\theta = -[w]_\times \delta\theta - \delta w_b - w_n \tag{14}$$

After performing the aforementioned operations, the differential equation describing the error state δx is obtained. Subsequently, a first-order expansion is performed to derive the state update equation.

$$\delta x = \delta x + \dot{\delta} x = (I + F\Delta t)\delta x \tag{15}$$

In the aforementioned differential equation, there are additional variables such as $a_n, and w_n$. Since the error values of the acceleration and angular velocity biases are unknown, random noises $a_w and b_w$, are introduced for these variables. All these variables serve as input variables U. During the state update process, in addition to the state transition matrix, there is also the driving matrix.

$$\delta x = (I + F\Delta t)\delta x + F_i U \tag{16}$$

With the state transition matrix and the driving matrix, the equations for state transitions and covariance updates can be derived.

$$P = (I + F\Delta t) P (I + F\Delta t)^T + F_i Q F_i^T \tag{17}$$

3.2. Autonomous positioning of drones using multi-source data fusion

The autonomous positioning method for drones used in bridge area inspection is illustrated in **Figure 2**. The process starts with raw data acquisition, bridge inspection surveys, and customized inspection task planning. Subsequently, multi-source sensors are utilized to obtain a three-dimensional (3D) digital terrain model, orthophotography imagery, and 3D spatial position data of the bridge. Next, by fusing multi-source data, including laser point clouds, multi-camera visible light imagery, and depth measurements, the inspection route is accurately determined. Finally, an integrated navigation and positioning algorithm combining GNSS, SINS (Strapdown Inertial Navigation System), RTK, LiDAR odometer, and visual odometer is adopted to achieve autonomous positioning.

The deeply coupled information fusion state quantity incorporates all relevant errors, resulting in the following filtered result:

$$X = \begin{bmatrix} \delta v_x, \delta v_y, \delta v_z, \delta L, \delta\lambda, \delta h, \phi_x, \phi_y, \phi_z \\ \varepsilon_x, \varepsilon_y, \varepsilon_z, \nabla_x, \nabla_y, \nabla_z, \delta t_u, \delta t_{ru} \end{bmatrix}^T \tag{18}$$

In the formula, the distance corresponding to the clock phase error is t_u ; the rate of change of distance corresponding to the clock frequency drift error is t_{ru} ; the attitude angle errors are represented by ϕ_x, ϕ_y, ϕ_z ; the latitude, longitude, and altitude errors are $L,, h$ respectively, the values $\varepsilon_x, \varepsilon_y, \varepsilon_z$ and $\nabla_x, \nabla_y, \nabla_z$ all represent random drifts, corresponding respectively to the gyroscope and accelerometer.

The pseudo-range deviation, pseudo-range increment deviation, and pseudo-range rate increment deviation in deep-coupled observations are denoted as δρ 、 δρ′ and respectively; all three quantities are derived from the pre-filter outputs of individual channels, enabling the calculation of navigation state parameter errors. The information output from the i-th tracking channel is given by Equation (19).

$$Z^i = \begin{bmatrix} \delta\rho^{\mathrm{i}} \\ \delta\Delta\rho^i \\ \delta\Delta\rho'^i \end{bmatrix} = \begin{bmatrix} \delta\rho \\ \delta\rho' \cdot T \\ \delta\rho'' \cdot T \end{bmatrix} \tag{19}$$

N denotes the number of following channels, and 3N represents the dimensionality of the observation information; thus, the observations for each channel are given by Equation (20).

$$Z = \begin{bmatrix} \delta\rho^1 & \cdots & \delta\rho^N & \cdots & \delta\Delta\rho^1 & \cdots & \delta\Delta\rho^N & \cdots & \delta\Delta\rho'^1 & \cdots & \delta\Delta\rho'^N \end{bmatrix}_3^T \tag{20}$$

On this basis, to minimize the integration time, let $t = t_2 - t_1$ represent the time interval, and e_j^T denote the navigation error. For the minimized integration, the pseudorange increment deviation formula is given by Equation (21).

$$\delta\rho^{\,i} = \rho_{INS}^j - \rho_{GPS}^j = e^T \cdot \delta r - \Gamma_{\delta p} \cdot \delta\rho_{rc} \tag{21}$$

In the formula, the clock coefficient matrix is denoted as $\Gamma_{\delta p}$, where $\Gamma_{\delta p} = [1, 0, 0]$.

On this basis, to minimize the integration time, let $t = t_2 - t_1$ represent the time interval, and since this involves minimizing the integral, the formula for the pseudo-range increment deviation is given in Equation (22).

$$\begin{aligned} \delta\Delta\rho^i &= \int_{t_1}^{t_2} \left(\dot{\rho}_{INS}^i - \dot{\rho}_{GPS}^i \right) dt \\ &= \left(\rho_{INS}^i (t_2) - \rho_{INS}^i (t_1) \right) - \left(\rho_{GPS}^i (t_2) - \rho_{GPS}^i (t_1) \right) \\ &= \Delta\rho_{INS}^i - \Delta\rho_{GPS}^i \\ &= e_i^T (t_2) \delta r (t_2) - e_i^T (t_1) \delta r (t_1) - \left(\delta r_u (t_2) - \delta r_u (t_{12}) \right) \end{aligned}$$

$$\begin{aligned} \delta\Delta\rho^i &= \int_{t_1}^{t_2} \left(\dot{\rho}_{INS}^i - \dot{\rho}_{GPS}^i \right) dt \\ &= \left(\rho_{INS}^i (t_2) - \rho_{INS}^i (t_1) \right) - \left(\rho_{GPS}^i (t_2) - \rho_{GPS}^i (t_1) \right) \\ &= \Delta\rho_{INS}^i - \Delta\rho_{GPS}^i \\ &= e_i^T (t_2) \cdot \delta r (t_2) - e_i^T (t_1) \cdot \delta r (t_1) - \left(\delta r_u (t_2) - \delta r_u (t_{12}) \right) \end{aligned} \tag{22}$$

Based on the dynamic linear recursive model and coordinate space variations, Equations (23) and (24) were derived.

$$\delta r(t_2) = \delta r(t_1) + \Delta t \delta v(t_2) + \frac{1}{2}\Delta t^2 \delta a(t_2) \tag{23}$$

$$a = C_b^{eb} \cdot \nabla^b + \tilde{a} \cdot \varphi \tag{24}$$

In the formula, the transformation matrix from the inspection drone's coordinate system to the Earth's coordinate system is C_b^e, the acceleration error is δa, the zero bias of the accelerometer's three axes in the drone's coordinate system is ∇^b, and the antisymmetric matrix of a is $\tilde{a}$. Substituting Equations (23) and (24) into the pseudorange increment deviation expression yields Equation (25):

$$\begin{aligned}\delta\Delta\rho^i = &\left(e_i^T(t_2) - e_i^T(t_1)\right)\cdot\delta r(t_2) + \Delta t \cdot e_i^T(t_1)\cdot\delta v(t_2) + \frac{1}{2}\Delta t^2 \cdot e_i^T(t_1)\cdot\delta a(t_2) \\ &+\frac{1}{2}\Delta t^2 \cdot e_i^T(t_1)\tilde{a}\varphi(t_2) + \frac{1}{2}\Delta t^2 e_i^T(t_1) C_b^e \cdot \nabla^b(t_2) - \Gamma_{\delta p}\delta\rho_{rc}(t_2)\end{aligned} \tag{25}$$

In the formula: $\Gamma_{\delta p} = \left[0, t, \frac{1}{2}t^2\right]$。

To obtain the pseudorange rate increment deviation, the same derivation method is applied, as shown in Equation (26).

$$\begin{aligned}\delta\Delta\rho^i = &\left(e_i^T(t_2) - e_i^T(t_1)\right)\cdot\delta v(t_2) + \Delta t \cdot e_i^T(t_1)\delta a(t_2) \\ &+\Delta t \cdot e_i^T(t_1)\tilde{a}\varphi(t_2) + \Delta t \cdot e_i^T(t_1) C_b^e \nabla^b(t_2) - \Gamma_{\delta p}\rho_{rc}(t_2)\end{aligned} \tag{26}$$

In the formula: $\Gamma_{\delta p} = [0, 0, \Delta t]$ Building on this foundation and incorporating the calculation procedures for pseudorange deviation, pseudorange increment deviation, and pseudorange rate increment deviation described above, the observation matrix (27) is derived.

$$Z = HZX = HX \tag{27}$$

In the formula, H denotes the output matrix, e represents the aerial survey error vector, and E denotes the aerial survey error matrix, with their expressions given in Equations (28) and (29).

$$H = \begin{bmatrix} E & 0_{n\times3} & 0_{n\times3} & 0_{n\times3} & 0_{n\times3} & 0_{n\times3} & -\Gamma_{\delta p} \\ \Delta E & \Delta t \cdot E_1 & \frac{1}{2}\Delta t^2 E_1 & \frac{1}{2}\Delta t^2 E_1 \tilde{a} & 0_{n\times3} & \frac{1}{2}\Delta t^2 \cdot E_1 \cdot C_b^e & -\Gamma_{\delta p} \\ 0_{n\times3} & \Delta E & \Delta t \cdot E_1 & \Delta t \cdot E_1 \tilde{a} & 0_{n\times3} & \Delta t \cdot E_1 C_b^e & -\Gamma_{\delta p} \end{bmatrix} \tag{28}$$

$$E = \begin{bmatrix} e_1^T(t_2) \\ \vdots \\ e_n^T(t_2) \end{bmatrix}, \quad E_1 = \begin{bmatrix} e_1^T(t_1) \\ \vdots \\ e_n^T(t_1) \end{bmatrix} \quad \Delta E = E - E_1 \quad \Delta t = T \tag{29}$$

By using the above algorithm to conduct deep coupling combination positioning of multi-source data, it can effectively reduce the influence of various abnormal interferences on the aerial survey errors, thereby providing continuous, smooth, and high-precision high-frequency position and attitude information for the inspection of an uncrewed aerial vehicle, enabling it to achieve autonomous positioning.

3.3. Autonomous following and obstacle avoidance of uncrewed aerial vehicles based on multi-source data fusion

The autonomous following and obstacle avoidance of uncrewed aerial vehicles (UAVs) based on multi-source data fusion all follow the core logic of "perception–processing–decision–control". They rely on multiple sensors (e.g., LiDAR and visible light sensors) as well as edge/embedded computing units to achieve autonomous inspection operations. The autonomous following path algorithm adheres to the process of "data acquisition–processing–decision–control", as illustrated in **Figure 3**. It first acquires point cloud data via LiDAR, updates the global point cloud through pose compensation, and completes data classification. Then, it combines feedback from multiple sensors to calculate the relative pose between the UAV, the bridge, and obstacles, and inputs the results into the PID algorithm to generate control commands, ensuring accurate path tracking. When the distance between the UAV and obstacles is less than the safety threshold, obstacle avoidance adjustment is triggered. Meanwhile, it completes core tasks such as deep-coupled pose calculation and global map construction, which breaks away from manual control, improves navigation accuracy and robustness, and solves the problem of reliance on highly reliable mobile digital networks. The obstacle avoidance system follows the logic of "real-time perception - data processing - decision control - route optimization". It acquires environmental information through laser scanning, generates global point clouds via parsing and pose compensation, and uses a classifier to identify obstacles and calculate their relative positions to ensure a safe distance. It adopts octree + bounding box to efficiently judge collisions, iteratively eliminates risks to optimize the route, and relies on the complementarity of visual images and LiDAR data. Through multi-step improvement strategies and sequential processes, it further enhances the safety and reliability of obstacle avoidance in complex environments.

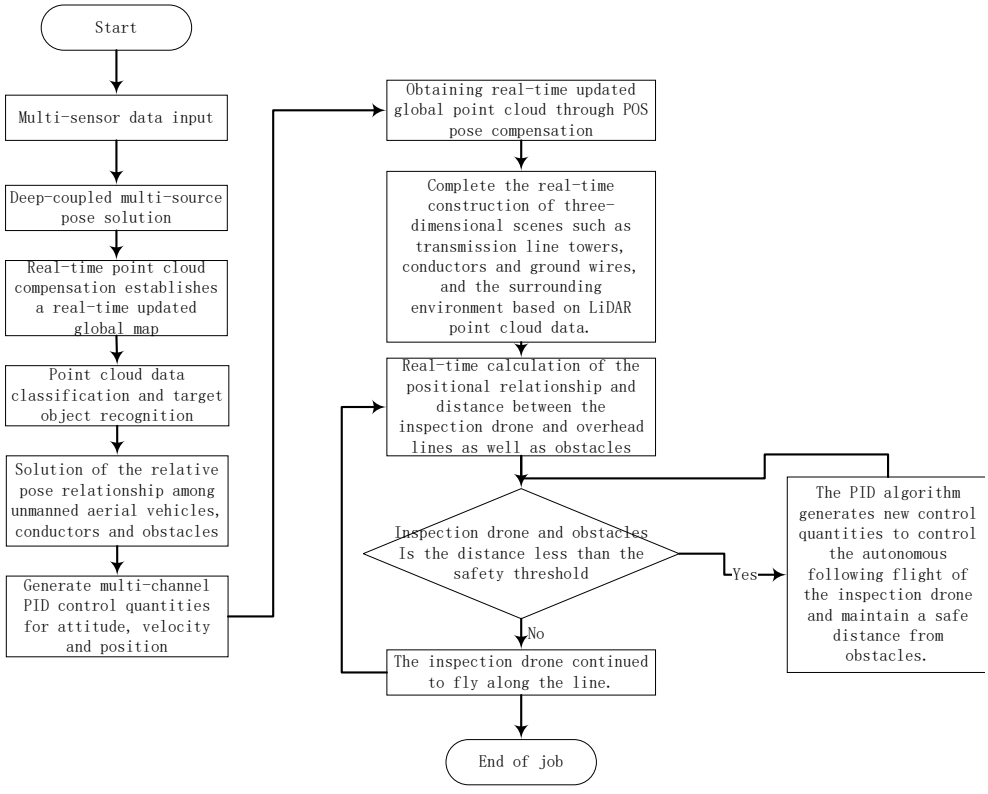

Figure 3. Autonomous obstacle avoidance of drones with multi-source data fusion.

The precise calculation of the optimal safe flight path for inspection UAVs serves as the core technical support for ensuring flight safety, minimizing battery consumption, and enhancing inspection efficiency and quality. Autonomous route planning must comprehensively consider multiple factors, including bridge structural orientation, equipment target point extraction, shooting position optimization, obstacle spatial positioning, and compliance with inspection regulations. The inspection route of a UAV is essentially a continuous vector line formed by connecting discrete flight nodes. The calculation process comprises two core components: safety verification of flight points and virtual three-dimensional scene space analysis. By integrating the camera parameter values of the inspection UAV, the camera positions corresponding to all shooting target points are calculated; meanwhile, safety avoidance factors are incorporated to generate the optimal safe inspection path for the UAV automatically. As illustrated in **Figure 4**, this is the flowchart of the optimal safe inspection path for inspection UAVs.

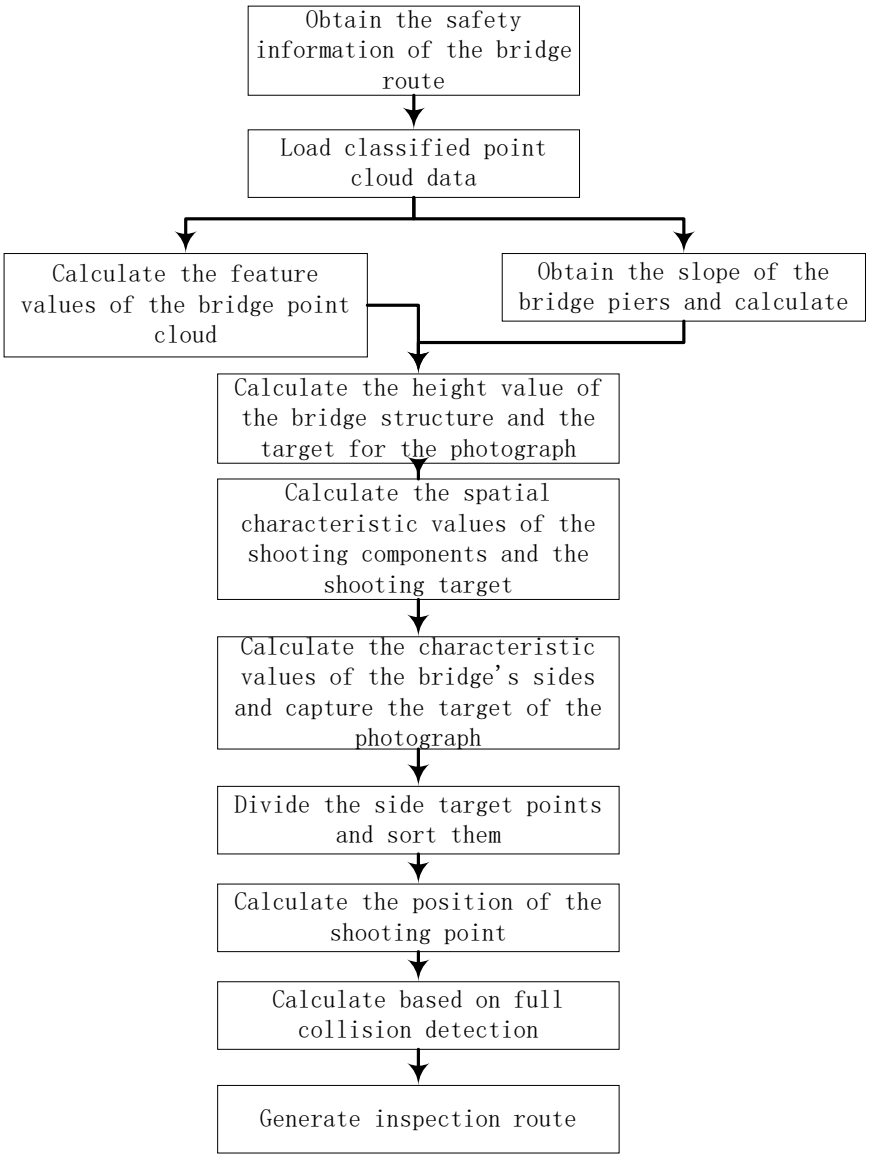

Figure 4. Optimal safety inspection path.

During path generation, the coordinates of the center point (x, y) of bridge piers are obtained through point cloud numbering matching. The octree structure is adopted to optimize the loading efficiency of point cloud data. Based on elevation values, key components such as pier tops, bridge decks, bridge foundations, and passages are accurately identified and stored. Subsequently, the horizontal distance of the target point is calculated using characteristic points at the bottom of the bridge piers, and the arc value is solved by combining the slope of the bridge deck to determine the rotation angle. Finally, the bridge reference height is acquired based on the midpoints of the bridge piers and map feature points, and the optimal flight altitude is generated through the coupling operation of the relative height (x, y) and the rotation angle.

$$\begin{cases} x_{new} = x\cos\alpha - y\sin\alpha \\ y_{new} = x\sin\alpha - y\cos\alpha \end{cases} \tag{30}$$

Based on this height value, we further calculate the (x, y) coordinates and side-channel dimensions of other bridge imaging components; classify the side target points according to the crossbeam orientation and sort them by the elevation z-value. The z-value of the camera position is determined using the difference between the z-value of the tower top and the bridge height, while the z-values of all bridge safety points are uniformly calibrated to this z-value. Finally, with the center point (x, y, z) of the target component as the reference, the relative rotation point is calculated. Through rotational transformation relative to the camera's center point, camera attitude parameters tailored to the inspection requirements are generated. The specific calculation method involves first calculating the radial deviation angle r:

$$\begin{cases} r = \dfrac{\pi}{4}, ifr \geq \dfrac{\pi}{2} \\ r = -\dfrac{\pi}{4}, \quad ifr < -\dfrac{\pi}{2} \end{cases} \tag{31}$$

Calculate the distance d to the target point:

$$d = dcosr \tag{32}$$

Calculate the position of the shooting point:

$$Prot(x, y, z) = (x - dtanr, y + d, z) \tag{33}$$

Calculate the coordinates (x, y) of the plane center:

$$Surface(x, y) = (x + dsinr, y - dcosr) \tag{34}$$

Calculate the side length of the plane:

$$Side = 0.01 * DIS_{pp} \tag{35}$$

Calculate the (x, y, z) coordinates of the four corners of the plane:

$$vfa_1(x, y, z) = Surface(x, y, z) + \left(-\frac{Side}{2}cosr, -\frac{Side}{2}sinr, -\frac{Side}{2} \right) \tag{36}$$

$$vfa_2(x, y, z) = Surface(x, y, z) + \left(\frac{Side}{2}cosr, \frac{Side}{2}sinr, -\frac{Side}{2} \right) \tag{37}$$

$$vfa_1(x,y,z) = Surface(x,y,z) + \left(\frac{Side}{2}cosr, \frac{Side}{2}sinr, \frac{Side}{2}\right) \tag{38}$$

4. Experimental verification

The simulation experiment adopts the partial reconstruction model of the Maqiao Railway and Road Overpass on the X103 County Road section from Jiaxing to Haining. The main parameters are presented in **Table 1**. The model effect of the bridge is illustrated in **Figure 5**, and the on-site photograph is shown in **Figure 6**.

Table 1. Main data of the bridge model

Bridge model	Length (m)	Wide (m)	High (m)	Pier diameter (m)
Golden Gate Bridge	401.664	57.9986	136.0021	\
Maqiao public-rail overpass	400.5719	36.9958	17.5599	1.1

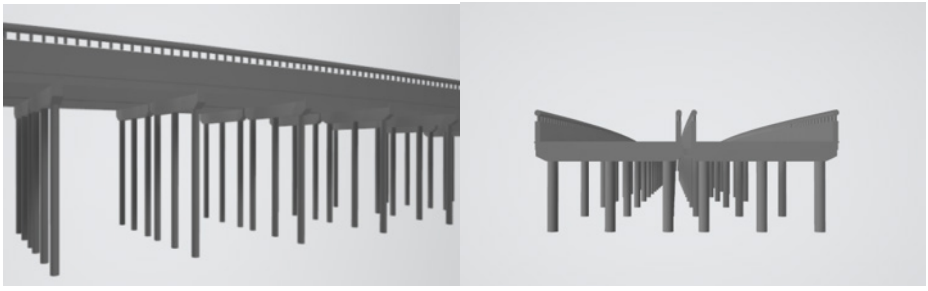

Figure 5. Partial model of the Maqiao public-rail overpass.

Figure 6. Actual photo of the Maqiao public-rail overpass.

Figure 7 represents the under-bridge route of the uncrewed aerial vehicle (UAV), while the global point cloud of under-bridge route planning is provided in **Figure 8**. Given a minimum planning time interval of 0.10 s, a maximum control input time interval of 0.15 s, a time spent on re-planning the path of 1.5 s, and a time per path segment of 0.15 s, the UAV could be put into a steady cruise state and would achieve good quality path planning, tracking, and obstacle avoidance. Assuming that the algorithm uses 4 GB of memory and 2 of the onboard computer cores, the full-range calculation of either the 30 m (x, y, z axes) or 100 m (x, y axes) ranges can be completed in less than 0.5 seconds and 1.5 seconds, respectively. The path planning was repeated five times consecutively at 30 m, 50 m, and 100 m, and none of them resulted in a collision. As

indicated in Table 2, the algorithm has a high-ratio initialization of the path planning, the average speed of the UAV flying is no more than 5 percent of the designed cruise speed, and the memory usage does not exceed 1/4 of the total memory of the onboard computer. All the measures are aligned with the design specifications, and other details, including the first planning time, are provided in **Table 2**.

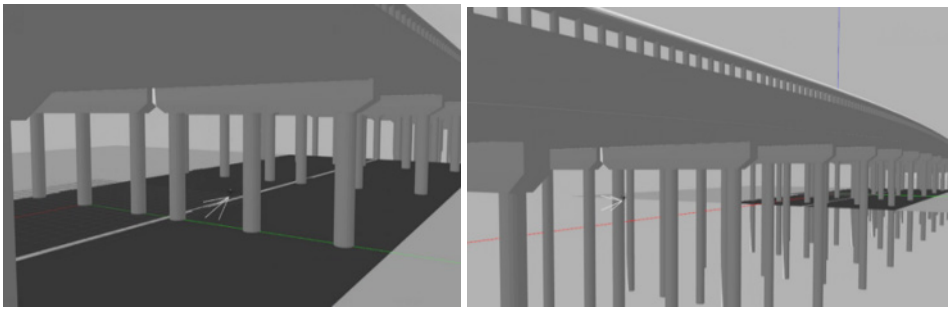

Figure 7. Inspection route under the bridge.

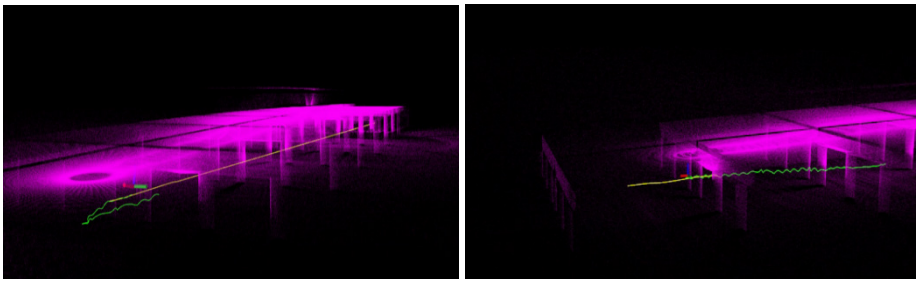

Figure 8. Global point cloud for path planning under the bridge.

Table 2. Experimental data on drone path planning performance

Project	Average initial path planning duration (s)	Average speed of the drone (m/s)	Average memory usage (GB)
30 meter	0.38	3.08	3.3
50 meter	0.61	2.95	3.6
100 meter	1.25	2.98	3.8

In the path planning experiments for 10 meters, 30 meters, 50 meters, and 100 meters, the frequency of collecting the UAV's motion information was 20 Hz. The maximum acceleration, average acceleration, yaw, pitch, and roll angular velocities, as well as angular accelerations of the UAV, are presented in Table 3. The maximum position error, average position error, maximum angle error, and average angle error of the UAV's path tracking are shown in **Table 4**. The calculation formulas for position error and angle error are as follows:

$$Err_{dis} = \sqrt[2]{pos_x^2 + pos_y^2 + pos_z^2} \tag{39}$$

$$Err_{deg} = \sqrt[2]{deg_{yaw}^2 + deg_{pitch}^2 + deg_{roll}^2} \tag{40}$$

Here, Err represents the error, pos represents the positional error, and deg represents the angular error.

Table 3. Experimental data on drone path planning performance

Project	Maximal acceleration m / s^2	Average acceleration m / s^2	Maximum yaw angular acceleration deg/s²	Maximum pitch angle acceleration deg /s²	Maximum roll angle acceleration deg /s²	Average yaw angle acceleration deg /s²	Average pitch angle acceleration °/s²	Average roll angle accelera tiondeg /s²
10 meter	1.27	0.45	13.1	8.1	4.3	1.5	0.12	0.24
30 meter	1.28	0.31	13.3	8.2	5.1	1.2	0.08	0.17
50 meter	1.25	0.28	13.5	7.9	4.8	0.8	0.06	0.12
100 meter	1.31	0.11	12.8	8.5	4.9	0.9	0.15	0.35

Table 4. Experimental data on drone path planning error

Project	Maximum positional error(cm)	Average Position Error (cm)	Maximum angular error(°)	Average Angle Error (°)
10 meter	4.1	1.7	13.3	4.2
30 meter	4.2	1.8	12.7	3.3
50 meter	3.9	1.7	14.2	3.1
100 meter	4.1	1.8	13.6	3.5

The maximum acceleration shown in **Table 3** is not much affected by the length of the path, and it remains stable at 1.25–1.31 m/s^2. Nevertheless, average acceleration drops dramatically as the length of the path increases, and this means that the smoothing of the path is increasing gradually. The biggest angular accelerations of yaw, pitch, and roll have fixed differences within the allowable limits, i.e., the spatial dynamics of the trajectory can be controlled. Mean yaw acceleration reduces slightly as the length of the path increases, but is quite low. Average pitch acceleration is constant at 0.06–0.15 deg/s^{2,} and average roll acceleration is maintained at 0.12–0.35 deg/s^2. There is no doubt at all that the UAV has an extremely high degree of flight acceleration control and great smoothness of the path in all lengths of the path. The path tracking algorithm controls the attitude variations of the UAV, preventing abrupt angle changes. The UAV is flown on long-distance missions, and the implementation of the inspection mission is also provided.

As shown in **Table 4**, the greatest position error does not differ much at the distance of 3.9–4.2 cm, and the average position error is in the range of 1.7–1.8 cm. It suggests that the UAV will accurately follow the designed path irrespective of the magnitude of the path. The whole interval of the maximum angle error is about 12.7–14.2 degrees, and the average angle error by increasing the length of the path is reduced by some 3.1–4.2 degrees, which shows that the path tracking algorithm is very consistent and reliable. These findings suggest that the path tracking algorithm can track the required path with a minimum displacement deviation, and the UAV angle error can be minimized at various lengths of the path, and it could be stabilized to the necessary flight attitude.

In order to investigate the signal attenuation properties of GNSS in the region of the road and bridge, the UAV was flown across the 20-meter-long bridge longitudinally. The line graph shown in Figure 9 was created by taking satellite counts that are visible at 20 points of flight (every 1.5 meters apart), starting at 15 m upstream and ending at 25 m downstream of the bridge (more than 60 meters). Those findings imply that when entering the bridge portion, the count of visible satellites reduced linearly by 25 (open area) to the least possible level in the middle of the bridge and increased back to normal with the approach to the end of the bridge, which means that there was a very clear V-shaped attenuation. Data presented in **Figure 10** is very

relevant to the tendencies of the theoretical curve, and the position of the minimum signal under the bridge can be explained by the predictions of the model. This indicates that the shielding impact of road and bridge infrastructure on the signals of the GNSS has been confirmed and provides a quantitative evaluation of the correction of the signals in the future.

Figure 10 shows a comparison of the results obtained by using planar position multi-source fusion and the first GPS data. The X / Y-axis curves indicate that the blue line (multi-source fusion trajectory) is less curved than the green GPS trajectory because it can be used effectively to delete discrete noise in the 1200-1400-step range and yet maintain the overall trend. This description is consistent with the probable kinematics constraints that corroborate the fact that inertial navigation is supplementary when a loss of positioning occurs over a short period.

At the moment when the dynamic changes occur on the velocity comparison plot given in **Figure 11**, the blue X/Y-direction velocity curve (multi-source fusion) and the green GPS velocity measurement curve have very high levels of synchronization. In acceleration transition areas, the fusion curve is quicker to respond as it benefits from the application of high-frequency IMU data fusion; in steady-state flight, the velocity estimate standard deviation has decreased by about 42 percent relative to GPS, which can be used to prove that multi-source data fusion can help decrease noise.

The attitude estimation development can be seen in the Euler angle curve in F**igure 12**. Predictably, the roll/pitch (red/blue lines) remained relatively constant during the course of the experiment, with an amplitude of about 400 (flying at the level altitude using a UAV), and the yaw angle (cyan line) gradually deviated by about 800 across 2,000 steps. It could have been caused by the presence of geomagnetic interference or an error in gyroscopic zero bias estimation, which will be discussed in the next plot of deviations.

The estimation of the zero bias of the gyroscope is depicted in **Figure 13**. During the initial phases of initialization, the three-axis deviation values converge relatively quickly (in less than 200 steps), and the X/Y axis converges to a constant value between the range of -0.002 to 0.002 rad/s while the Z axis is continuously drifted at about 0.004 rad/s. This discrepancy in axes may be explained by the installation or coupling of IMU torque due to vibrations of the carriers. The mechanical fixation condition should be checked, and the parameters of the process noise should be optimized through the use of the Kalman filter algorithm.

As shown in **Figure 14**, the time-varying property of accelerometer drift varies. The zero drift of the axis-X is affected by a change of a step of 0.1 m/s² at 1,200 steps, which coincides with the duration of the strong side wind perturbation observed in the experimental log and indicates that dynamic tracking may be used to determine the environmental coupling errors in carrier acceleration. In contrast, the Y/Z-axis zero drift is extremely stable, and its variations are less than 0.04 m/s², which can be regarded as an anti-interference property of redundant IMU design.

Figure 15 is the comparison of the degree of closure of the trajectory. When the two paths are merged (in red), they have a higher level of closure and coherence with respect to geometry than the original GPS path (in green). In particular, in the southeastern quadrant (X > 40 m), it would be able to correct the deviation of the GPS data rather well, and the standard deviation of the trajectory would decrease by 1.2 m to 0.34 m. It has been found that the reliability of integrated navigation systems has significantly increased in the conditions of complex electromagnetic environments. Nevertheless, there still is an error of about 0.8 m in the northeast corner (X = 120 m and Y = 80 m).

The effectiveness of multi-dimensional data integration has been established through an experiment where multi-dimensional data were compared. The indicated algorithm showed an excellent result in terms

of the smoothness of the position, the reduction of speed noise, dynamism, and the resistance to interference because it was very instrumental in improving the reliability of navigation in a complex environment. Nonetheless, yaw angle drift, Z-axis gyroscope zero bias drift, and local trajectory residuals were noted. It is thought that these are related to geomagnetic interference, mechanical installation, and filtering parameters. It is necessary to optimize the fixed connection state and filtering parameters further to improve the accuracy and stability of navigation. See **Figure 16**.

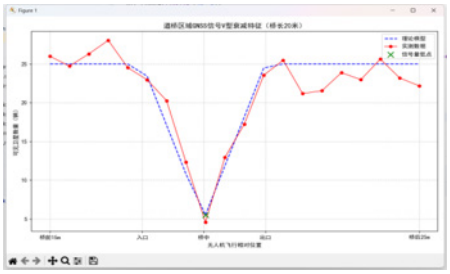

Figure 9. GNSS signal variation.

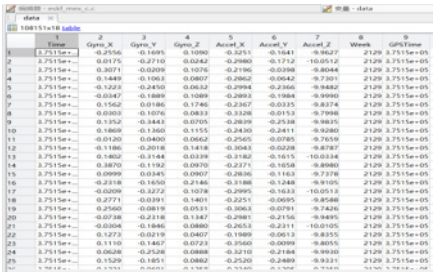

Figure 10. Collected data.

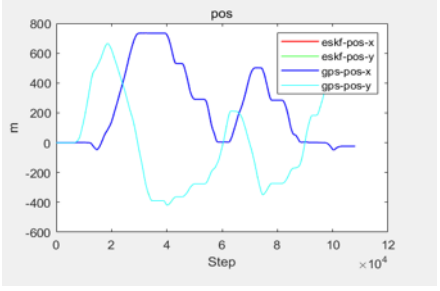

Figure 11. Position Comparison Diagram.

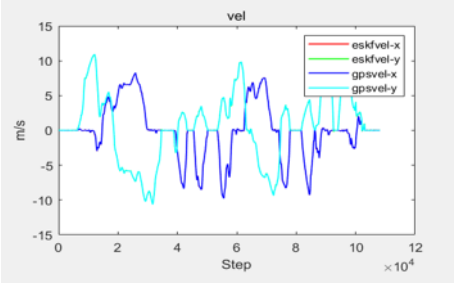

Figure 12. Speed comparison.

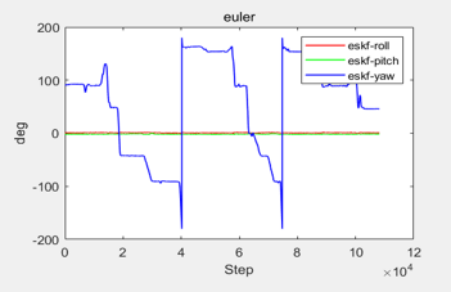

Figure 13. Posture angle analysis.

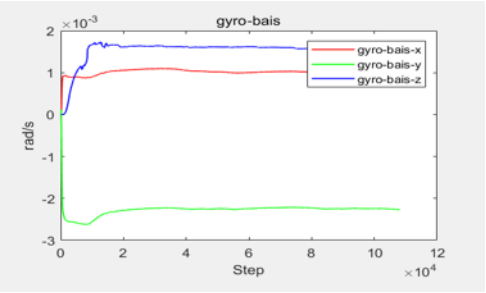

Figure 14. Gyroscope zero bias estimation.

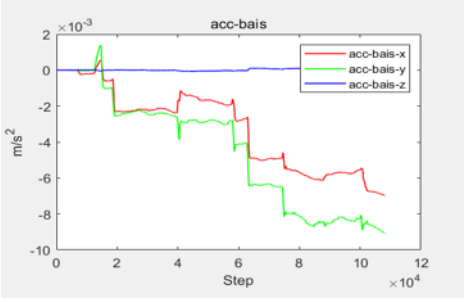

Figure 15. Accelerometer drift analysis.

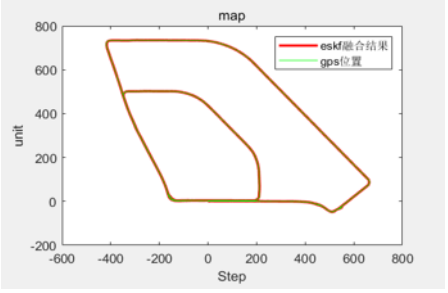

Figure 16. Comparison of trajectory closure degree.

5. Conclusion

In order to meet the first requirement of the extremely accurate navigation and positioning of drones in the bridge situation, the current paper will discuss the natural properties of low-altitude objects in the indicated

situations and perform a thorough analysis of the technical problems associated with the distinctive structure of bridges and the intricacies of their conditions. Such environments tend to be problematic, especially when the signals become blocked, position drift occurs, and errors accumulate, especially within more complex areas of structures like the deck of a bridge, the shaded areas, or even the steel truss bridges, wherein traditional single-navigational systems cannot fulfill the need for high precision positioning to provide constant drone flight. An information fusion navigation system that incorporates the Global Navigation Satellite System (GNSS), Inertial Navigation System (INS), coupled with visual sensors and Lidar, is an efficient tool to disrupt the underlying technical bottleneck of the transience of navigation signals, creating additional coordination systems and dynamic adaptation strategies of heterogeneous navigation data. It has a huge positive effect on the precision of positioning and stability of navigation of drones in complex structured environments. The suggested solution offers technical safety of drones performing autonomous operations in the course of bridge inspection and repair activities that increase the variety of use of drones in adverse engineering conditions and prove their significant practical value with numerous opportunities for application.

Funding

Scientific Research Fund of Zhejiang Provincial Education Department (Project No.: Y202558184); Scientific Research Fund of Hangzhou Dianzi University Information Engineering College (Project No.: KYP0324006); National Training Program of Innovation and Entrepreneurship for Undergraduates (Project No.: 202513279019); Laboratory Research Project, College of Information Engineering, Hangzhou Dianzi University (Project No.: SYSYJ20250601)

Disclosure statement

The authors declare no conflict of interest.

References

[1] Cao Y, Li H, 2024, Experimental Research on Autonomous Localization of Unmanned Vehicles Based on Multi-sensor Fusion. Modern Electronic Technology, 47(16): 90–96.

[2] Huang Z, Liu Z, Luo P, et al., 2020, Research on Integrated Inertial Navigation System. Journal of Guangzhou Maritime University, 28(1): 43–48.

[3] Liu C, 2020, Research on Data Processing Algorithm of GNSS/INS Integrated Navigation and Positioning, thesis, University of Chinese Academy of Sciences.

[4] Huang T, 2022, Research on Nonlinear Filtering Algorithm and Its Application in Integrated Navigation, thesis, Nanchang University.

[5] Liu J, 2024, Research on Autonomous Positioning and Orientation Algorithm Based on GNSS/INS/Visual Integration, thesis, Xi'an University of Technology.

[6] Zhu Y, 2021, Research on Information Fusion of Redundant MEMS Inertial Navigation System, thesis, Hebei University of Technology.

[7] Cheng B, 2021, Research on Positioning of GNSS/Inertial Navigation Integrated System in Complex Environments. Journal of North University of China (Natural Science Edition), 42(1): 89–96.

[8] Li N, Guan L, Gao Y, et al., 2020, Indoor and Outdoor Low-Cost Seamless Integrated Navigation System Based on INS/GNSS/LIDAR Integration. Remote Sensing, 12(19): 3271.

[9] Jiang H, Li T, Song D, et al., 2022, An Effective Integrity Monitoring Scheme for GNSS/INS/Vision Integration Based on Error State EKF Model. IEEE Sensors Journal, 22(7): 7063–7073.

[10] Li X, Li S, Zhou Y, et al., 2022, Continuous and Precise Positioning in Urban Environments by Tightly Coupled Integration of GNSS, INS and Vision. IEEE Robotics and Automation Letters: 1–8.

[11] Zhang Q, Niu X, Shi C, 2020, Impact Assessment of Various IMU Error Sources on the Relative Accuracy of the GNSS/INS Systems. IEEE Sensors Journal, 20(9): 5026–5038.

[12] Wang Z, Liu J, Zhang W, et al., 2025, Adaptive Filtering Algorithm for UAV Integrated Navigation in Complex Environments. Transducer and Microsystem Technologies, 44(1): 135–140.

[13] Zhou Y, Zhou E, Hong Z, 2025, Anti-interference Positioning Based on Multi-sensor Fusion of Thermal Imaging, LiDAR and GNSS. Transducer and Microsystem Technologies, 44(1): 88–92.

[14] Zhao Y, Zhou W, Wang X, et al., 2026, Research on Robot Path Planning Based on Improved A-Star Algorithm. Modern Electronic Technology, 49(1): 148–156.